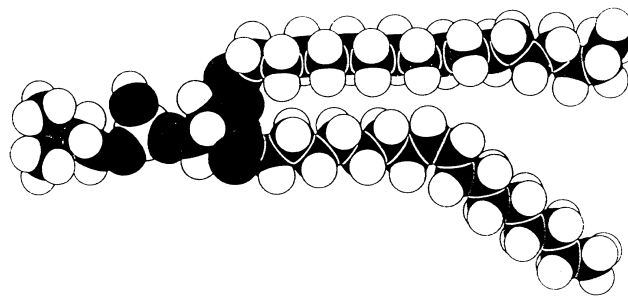


# **B 9 Coarse-Grained and Continuum Models of Membranes**

G. Gompper and H. Noguchi  
Institut für Festkörperforschung  
Forschungszentrum Jülich GmbH

## **Contents**

<b>1</b>	<b>Introduction</b>	<b>2</b>
1.1	Amphiphiles and Membranes . . . . .	2
1.2	Computer Simulations . . . . .	3
<b>2</b>	<b>Coarse-Grained Membrane Models</b>	<b>5</b>
2.1	Introduction . . . . .	5
2.2	Lennard-Jones and Dissipative-Particle-Dynamics Models . . . . .	6
2.3	Self-Assembly of Micelles and Bilayers . . . . .	7
2.4	Thermal Membrane Fluctuations . . . . .	9
<b>3</b>	<b>Solvent-Free Membrane Models</b>	<b>9</b>
3.1	Introduction . . . . .	9
3.2	Model and Simulation Methods . . . . .	11
3.3	Properties of Vesicles . . . . .	12
3.4	Membrane Fusion . . . . .	13
<b>4</b>	<b>Dynamically-Triangulated Surfaces</b>	<b>15</b>
4.1	Continuum Description and Curvature Elasticity . . . . .	15
4.2	Simulation Method . . . . .	15
4.3	Crumpling of Thin Elastic Sheets . . . . .	17
4.4	Vesicles and Red Blood Cells in Capillary Flow . . . . .	18
<b>A</b>	<b>Thermal Fluctuations of Nearly Planar Membranes</b>	<b>23</b>



**Fig. 1:** *Schematic representation of a lipid molecule — which consists of a polar head (left) and two hydrocarbon tails (right). The kink in one of the hydrocarbon chains, which is due to a C – C double bond, is important for the fluidity of the membrane.*

## 1 Introduction

### 1.1 Amphiphiles and Membranes

In Biophysical and Soft Matter Science, amphiphilic properties of molecules play a very important role in self-assembly and structure formation [1, 2, 3, 4, 5]. A molecule is called “amphiphilic” — from the Greek ‘loving both’ — when it consists of a hydrophilic (‘water-loving’) and a hydrophobic (‘water-fearing’) part. The most common amphiphilic molecules are surfactants, soaps and detergents, which consist of a polar head and a hydrocarbon tail. These molecules assemble at a water-oil interface to form monolayers, such that the hydrophilic polar head is placed in an aqueous environment, while simultaneously the hydrophobic hydrocarbon tail is located in the oil and avoids water contact.

Amphiphilic molecules also form the basic structural element of the membranes in biological cells, which includes both the plasma membrane (the ‘outer skin’ of the cell) as well as all cell organelles. In this case, a special class of amphiphilic molecules is almost universally found, which consists of a polar head and *two* hydrocarbon chains — the phospholipids. An example is shown in Fig. 1. The advantage of double-tail lipids compared to single-tail surfactants is that the molecular solubility of the former is much lower than of the latter, so that all lipid molecules are confined to membranes, and the membrane area does not change.

The structure of a biological membrane is shown schematically in Fig. 2. Its basic building block is the lipid bilayer, in which the hydrophobic tails are shielded from the contact with water by the two layers of hydrophilic head groups. A biomembrane is typically composed of many different lipids. This opens the possibility of phase separation and domain formation. In addition, a biological membrane contains a large number of trans-membrane proteins, which control the exchange of water, ions, and small molecules between the cell plasma and the extracellular space. The role of lipid domains, called “rafts”, in the functioning and control of membrane proteins has been investigated intensively in recent years [6].

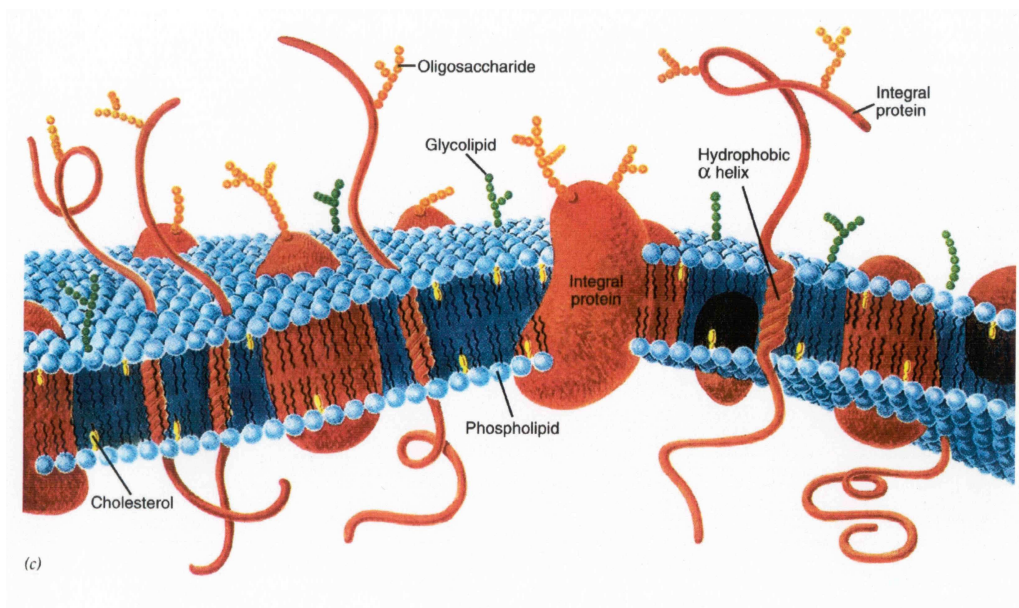


**Fig. 2:** Schematic representation of a biological membrane, which shows the lipid bilayer, cholesterol molecules embedded in it, as well as several types of trans-membrane proteins. From Ref. [7].

## 1.2 Computer Simulations

Computer simulations of the self-assembly of amphiphilic molecules into micelles (small spherical or cylindrical surfactant aggregates), monolayer and bilayers have a long history [8, 9, 10, 11, 12]. Since the physical effects in membranes cover such a large range of relevant length- and time-scales — from the quantum-mechanical behavior of motions in a single molecule and the hydrogen-bonds between different molecules to the hydrodynamic behavior of vesicles and cells — that no single computer model can capture them all, compare Fig. 3.

Therefore, several different models, which are suitable to study phenomena on a smaller range of length scales as illustrated in Fig. 4, have been developed over the last decades:

- **Microscopic Membrane Models** — On the microscopic scale, *all-atom simulations* are required, in which the positions of the atoms of all molecules as well as the interactions between them are modeled explicitly. The interactions sometimes treated quantum-mechanically, but in most cases by classical force fields. The reliability of the results of all-atom simulations strongly depends on the art to determine the force fields. All-atom simulations are indispensable whenever the chemical structure of the participant molecules is relevant for the phenomena under investigation. For example, the functioning of a membrane protein which acts as a ion pump can only be understood on the basis of such atomistic models. For more details see Chaps. B10 and B11.
- **Coarse-Grained Membrane Models** — If the detailed chemical structure is not relevant, but more generic properties of amphiphilic molecules are to be studied — like the number of hydrocarbon tails, the chain length of the tails, or mixtures of two different amphiphiles — then a *coarse-grained description* can be used, in which several atoms are lumped into a single unit. These units are typically taken to be hard spheres. In such a model, water becomes hard-sphere fluid with attractive interactions, and amphiphilic

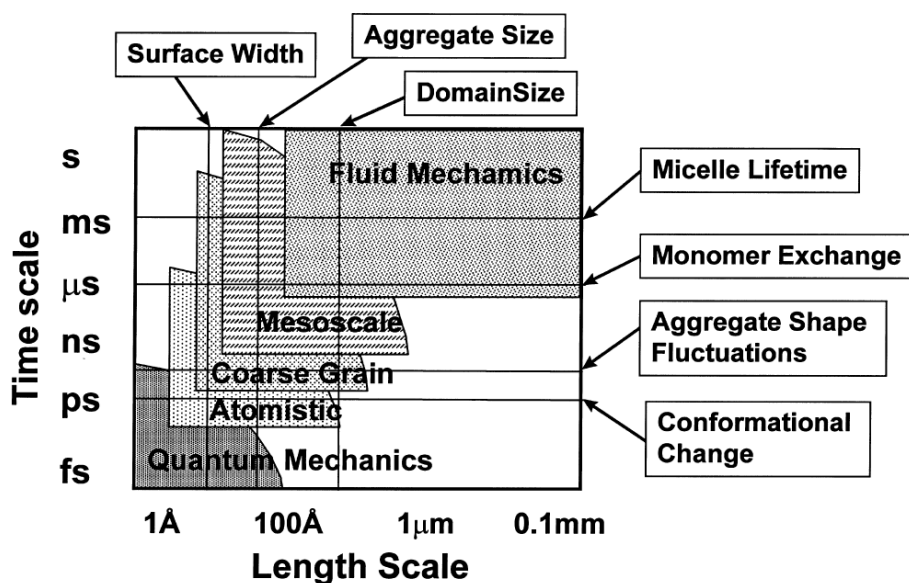


**Fig. 3:** Characteristic time and length scales in amphiphile solutions. Physical phenomena occurring at the various scales are indicated. Different models and simulation techniques are required to capture the behavior at different scales. Their approximate ranges of validity are shown by the shaded regions. From Ref. [12].

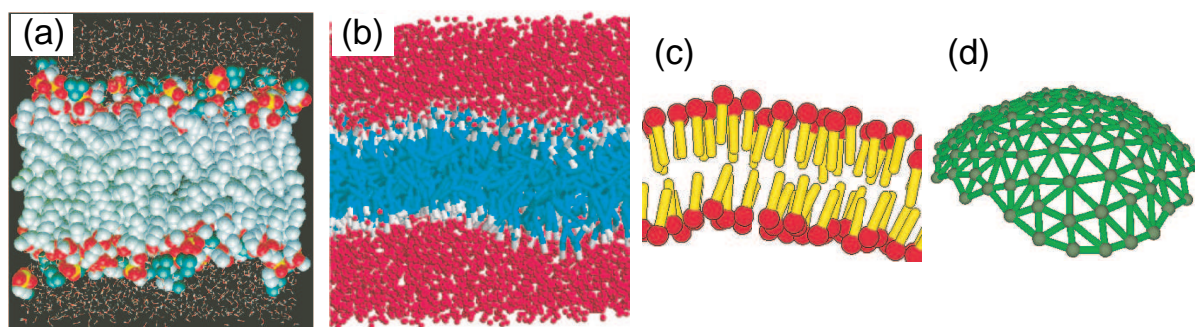


**Fig. 4:** Membranes models on different length scales. (a) Atomistic model (from Ref. [13]), (b) coarse-grained model (from Ref. [14]), (c) solvent-free bilayer model, and (d) triangulated surface model. Note that the characteristic length in these models is (a) a few Ångstroms, (b),(c) a few nanometers, and (d) tens to hundreds of nanometers.

molecules become chains of beads of two kinds, with attractive or repulsive interactions with the solvent beads. The size of such a bead is on the order of a few water molecules or  $CH_2$  groups.

- **Solvent-Free Membrane Models** — The solvent in a coarse-grained model is required for two reasons. First, it is necessary to stabilize the bilayer structure due to the repulsion between the solvent and the amphiphile tails. Second, it describes the hydrodynamic interaction between different parts of the membrane, which is mediated by the solvent. However, the simulation of the motion of the solvent particles consumes a large fraction of the total simulation time. Therefore, *solvent-free membrane models* have been designed, which work as well as the models with solvent when structural and thermodynamic properties are investigated. Additional interactions between amphiphiles have to be introduced in this case in order to mimic the hydrophobic interactions with the solvent.
- **Triangulated Surface Models** — The natural length scale of the previous two classes of membrane models is the size of the head group of a lipid molecule, i.e. it is roughly 1 nm. This is still far too small to describe phenomena on the scale of giant vesicles or cell, which have a diameter of about 10  $\mu\text{m}$ . In this case, a *continuum description* on the level of *elasticity theory* is required. The building block in such a model is a membrane patch consisting of hundreds or thousands of lipid molecules. In order to make this model amenable to computer simulations, *dynamically-triangulated surfaces* are usually employed.

## 2 Coarse-Grained Membrane Models

### 2.1 Introduction

When the detailed chemical structure of the amphiphilic molecules is not important, a coarse-grained modeling is very useful, where groups of several atoms or molecules are described by only a single position vector. This is important, since it

- reduces the number of degrees of freedom, and therefore allows either to study the system over a longer time range, or to study larger system sizes, or both;
- emphasizes the universal aspects, which are common to many different amphiphilic systems, independent of the detailed chemistry of a particular system.

This approach has been used to address a variety of questions recently, *inter alia*

- membrane self-assembly and structure [15, 16, 17, 18, 19, 20, 21],
- the spectrum of thermally excited membrane fluctuations [16, 18],
- phase diagrams of lipid bilayers [22],
- pore formation in membranes [23, 24, 25],
- domain-formation in multi-component membranes [26],
- membrane fusion [27, 28, 29, 30, 31].

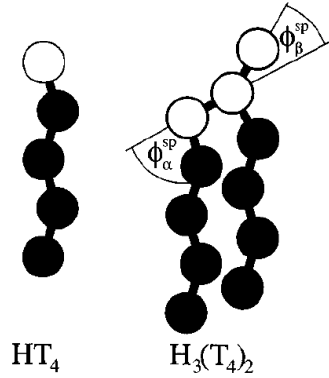


**Fig. 5:** Typical amphiphilic molecules used in coarse-grained membrane models. The white particles (*H*) represent the head group, the black particles (*T*) the tails. From Ref. [15].

## 2.2 Lennard-Jones and Dissipative-Particle-Dynamics Models

In coarse-grained models, the solvent molecules are treated as spherical particles with attractive Lennard-Jones interactions,

$$U_{LJ}(r) = 4\epsilon \left[ \left( \frac{\sigma}{r} \right)^{12} - \left( \frac{\sigma}{r} \right)^6 \right] \quad (1)$$

where  $\sigma$  is the (effective) hard-core radius. The amphiphilic molecules are modeled as short polymeric chains of head (*H*) and tail (*T*) particles, so that neighboring particles in the chain interact via the harmonic-spring potential

$$U_{chain}(r) = k_{chain}(r - \sigma)^2 \quad (2)$$

Different geometries of amphiphilic molecules are shown in Fig. 5. Head and tail particles also attract each other with the Lennard-Jones potential (1), as well as head and solvent particles. However, the tail particles have a *repulsive* interaction with both the head and the solvent particles. This interaction can be conveniently described by a shifted and truncated Lennard-Jones potential

$$U_{LJ}(r) = \begin{cases} 4\epsilon \left[ \left( \frac{\sigma}{r} \right)^{12} - \left( \frac{\sigma}{r} \right)^6 \right] + \epsilon & \text{for } r < 2^{1/6}\sigma \\ 0 & \text{otherwise} \end{cases}$$

which has the advantage of being continuous and differentiable at the cutoff  $r = 2^{1/6}\sigma$ . In this model, the Newton's equation of motion for all particle position are solved by a molecular dynamics simulation employing the velocity-Verlet algorithm [compare Chap. B3], where the mass  $m_0$  of all particles is assumed for simplicity to be the same.

An alternative approach to simulate coarse-grained membrane models is dissipate-particle dynamics (DPD) [17, 26, 30]. An introduction into the DPD simulation technique can be found in Chap. B5. In this case, the Lennard-Jones interactions between particles species are replaced by the conservative forces

$$\mathbf{F}_{ij}^C = a_{ij} (1 - r_{ij}/r_0) \hat{\mathbf{r}}_{ij} \quad (3)$$

for distances  $r_{ij} < r_0$  and zero otherwise. Similarly, the dissipative friction forces are taken to be

$$\mathbf{F}_{ij}^D = \gamma_{ij} (1 - r_{ij}/r_0)^2 (\hat{\mathbf{r}}_{ij} \cdot \mathbf{v}_{ij}) \hat{\mathbf{r}}_{ij} \quad (4)$$

interactions	$a_{ij}$	$\gamma_{ij}$
HH	25	4.5
TT	25	4.5
WW	25	4.5
HW	35	4.5
HT	50	9.0
TW	75	20.0

**Table 1:** Two-particle conservative force parameters  $a_{ij}$  (in units of  $k_B T/r_0$ ) and dissipative force parameters  $\gamma_{ij}$  (in units of  $\sqrt{m_0 k_B T}/r_0^2$ ) for all particle pairs.  $k_B T$  is the thermal energy. Here, ‘H’ denotes heads, ‘T’ tails, and ‘W’ solvent (water) particles. From Ref. [17].

for distances  $r_{ij} < r_0$  and zero otherwise, where  $\mathbf{v}_{ij} = \mathbf{v}_i - \mathbf{v}_j$  is their relative velocity. Finally, the thermal random force follows from the fluctuation-dissipation theorem, as explained in Chap. B5. A choice of interaction parameters, which leads to the formation of stable bilayers, is given in Tab. 2.2. All conservative forces are taken to be *repulsive*. Water is slightly repelled from the amphiphile head, and is strongly repelled from the amphiphile tail, which provides the hydrophobic interaction needed to form bilayers. The amphiphile head is hydrophilic and therefore repelled somewhat from its tail.

## 2.3 Self-Assembly of Micelles and Bilayers

The self-assembly of amphiphilic molecules in aqueous solution into a large variety of different structures is their most important property [2, 1]. The type of structure found depends very much on the amphiphile concentration, but also on the amphiphile architecture and on environmental conditions, such as temperature, salt concentration, etc.

At very small amphiphile concentrations, the amphiphiles are molecularly dispersed, since the translational entropy dominates over any interaction energy. Only when a minimal concentration — the *critical micelle concentration* (CMC) — is exceeded, the amphiphiles aggregate in small droplets called *micelles*, in which the hydrocarbon tails are shielded from water contact by a layer of head groups. The typical size of a spherical micelle is therefore determined by the length of the amphiphilic molecules. In some systems, when the size of the head group is larger than the tail, micelles can grow into long cylindrical rods which are called cylindrical micelles. On the other hand, when head and tail of the amphiphiles have roughly the same size, micelles can grow into two-dimensional bilayer patches. This can happen at still small amphiphile concentrations (above the CMC). In this case, the patch does not grow indefinitely in the lateral directions, because the rim of the patch is energetically less favorable than the interior. This can be understood as a line tension of the rim. Since the rim energy grows linearly with the radius of the patch, at some point the flat bilayer becomes less favorable a closed bilayer of roughly spherical shape, which is called a vesicle — compare Sec. 3.3 below. In contrast to micelles, vesicles can be much larger than the length of an amphiphile. *Giant vesicles* reach sizes of 10  $\mu\text{m}$  diameter, which is comparable to the size of biological cells.

At considerably higher amphiphile concentrations, micelles or bilayers pack together to form three-dimensional order phases, like cubic micellar crystals, or lamellar phases in which bilayers form a stack in one direction.

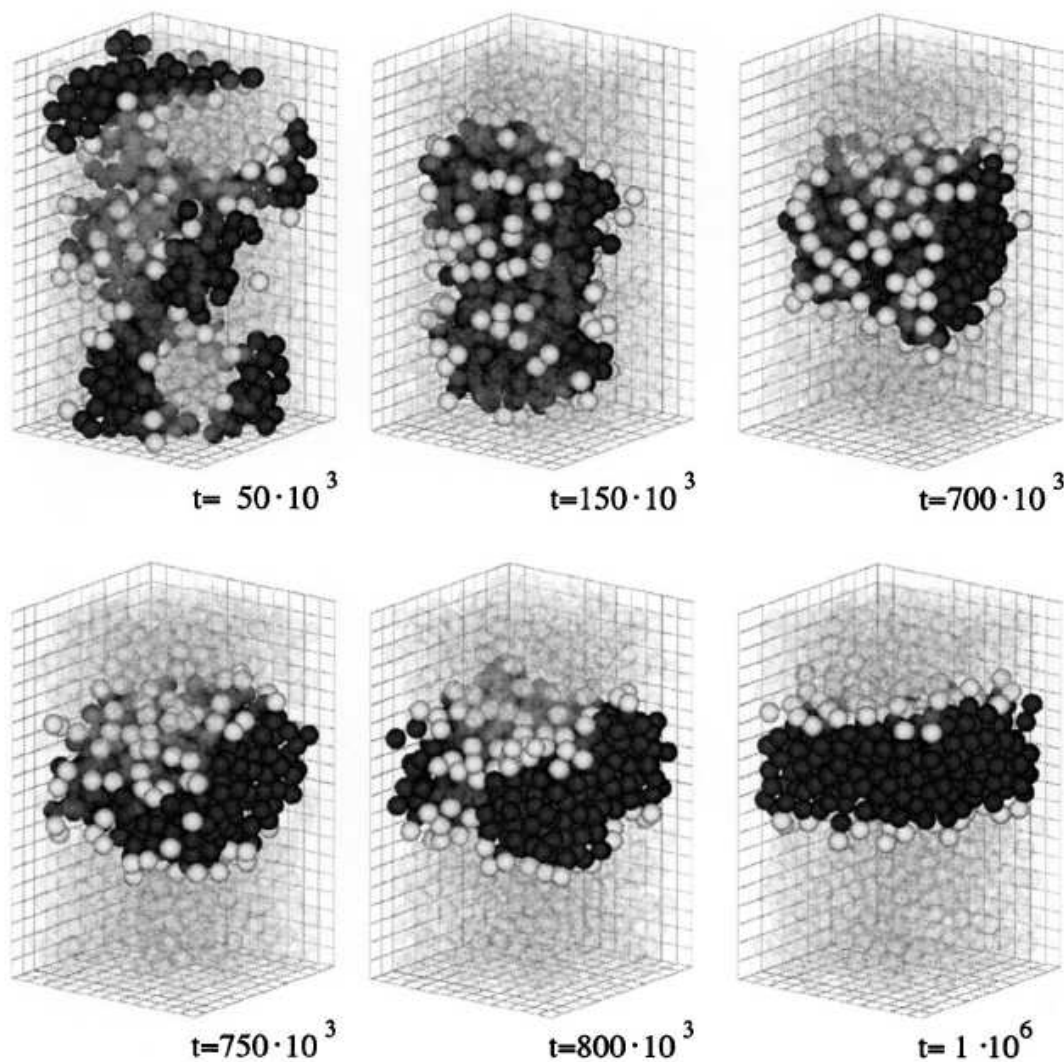


**Fig. 6:** Self-assembly of a bilayer membrane in a mixture of  $HT_4$  amphiphiles and solvent particles. The solvent particles are nearly transparent. The initial configuration, which is not shown, consists of a random mixture of 100 amphiphile and 840 solvent particles. The configurations are snapshots which illustrate the time evolution of the structure. After about  $10^5$  molecular dynamics (MD) time steps, the amphiphiles form a cylindrical micelle, which spans the simulation box horizontally. This state is metastable for some time, before it transforms into a stable bilayer structure. From Ref. [16].



Many aspects of this self-assembly process have been studied by simulations. One aspect, the formation of a bilayer from an initially random mixture of amphiphiles and water, as obtained from molecular dynamics simulations of the coarse-grained Lennard-Jones model of Sec. 2.2, is shown in Fig. 6. It shows the formation of a transient cylindrical micelle structure, which transforms after some time into a stable bilayer state. Note that due to the finite box size, the amphiphile concentration is rather large, so that this bilayer should be considered as a part of a lamellar phase.

## 2.4 Thermal Membrane Fluctuations

Thermal fluctuations of the lipid molecules in a membrane lead to two types of thermal excitations of a membrane, see Fig. 7b. On short length scales, the lipid molecules are not perfectly aligned and do not have their heads all in the same plane, but there are small vertical displacements between neighbors. These thermal motions are called *protrusion modes*. On the other hand, on length scales much larger than the bilayer thickness, there is a collective excitation, where the whole membrane displays a wave-like deformation, which is called an *undulation mode*. The amplitudes are accessible experimentally, for example by scattering techniques.

In order to determine the spectrum of fluctuation modes of a membrane in simulations, a scalar height variable  $h(\mathbf{r})$  is introduced, which measures the deviation of the *local* position of the amphiphile head from a planar reference state (Monge parametrization). The fluctuation spectrum is then obtained from the correlation function

$$S(\mathbf{q}) \equiv \langle |h(\mathbf{q})|^2 \rangle \quad (5)$$

where

$$h(\mathbf{q}) = \frac{1}{N} \sum_{i=1} h(\mathbf{r}_i) \exp(i\mathbf{q} \cdot \mathbf{r}_i) \quad (6)$$

with  $N$  the number of amphiphiles, is the two-dimensional Fourier-transform of the height-field  $h(\mathbf{r})$ .

The results are shown in Fig. 7a. For small wave numbers  $q$ , the spectrum shows a  $q^{-4}$  decay, which is characteristic for surface which are governed by the *curvature elasticity* (compare Sec. 4.1 below). The amplitude of this power law is the bending rigidity, which can thereby extracted from the simulations, as explained in more detail in Appendix A. This behavior should be compared with the spectrum of a surface governed by the surface tension (like the air-water interface), where the spectrum decays as  $q^{-2}$  for small wave numbers (see Appendix A). The spectrum for large wave numbers, on the other hand, follows a  $q^{-2}$  power-law. It is no coincidence that this is the same power law as for surfaces with surface tension, since the energy of the protrusion modes is proportional to the hydrophobic area exposed to the water when the amphiphiles “stick their head out” of the bilayer.

## 3 Solvent-Free Membrane Models

### 3.1 Introduction

Simulations of lipid membranes by molecular dynamics require the calculation of the motion of a large number of water molecules in addition to the lipid molecules. To simulate a small patch of a *flat* membrane with an atomistic model, about 30 water molecules per lipid were found to

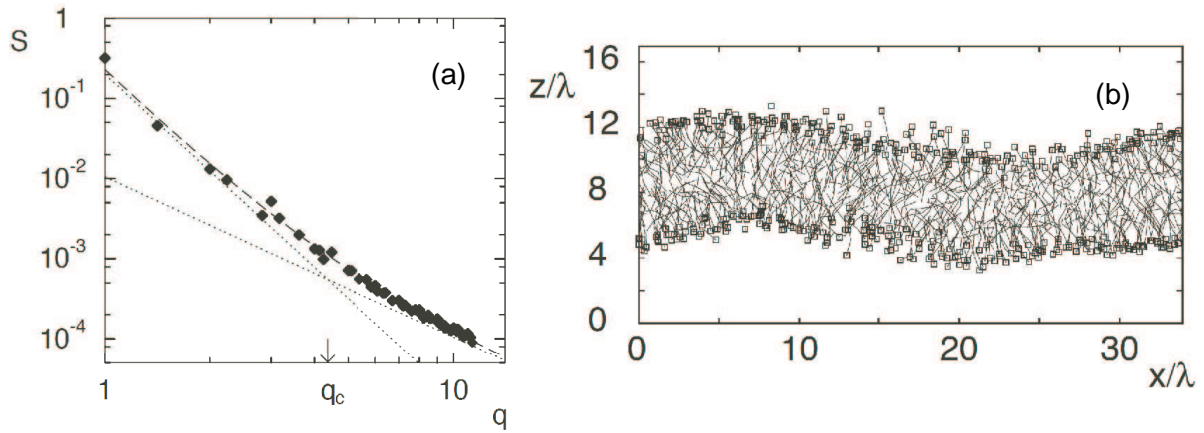


**Fig. 7:** *Fluctuation modes of thermally excited membrane deformations. (a) Fluctuation spectrum  $S = \langle |h(\mathbf{q})|^2 \rangle$  as a function of the dimensionless wave number  $q$ . The largest wave number is determined by the box size and corresponds to  $q = 1$ . The dotted lines show the expected power-law behavior due to undulations (small  $q$ ) and protrusions (large  $q$ ), respectively. (b) Typical configuration of a bilayer membrane composed of 1152  $HT_4$  amphiphiles. At small scales, individual molecules protrude from the bilayer. At large scales, the bilayer looks like an elastic, smoothly curved sheet. The basic length scale  $\lambda$  represents the range of the Lennard-Jones potential. From Ref. [16].*

be sufficient [13]. However, much more water molecules are needed for simulations of vesicles, since the formation of a vesicle [Fig. 8] needs a lot of solvent space to prevent membrane interactions through the periodic boundary conditions of the simulation box. The self-assembly of amphiphilic molecules in dilute solutions also requires a lot of water molecules.

In solvent-free models, the solvent is not taken into account explicitly. Instead, the solvent effect is treated by an effective potential between amphiphilic molecules. This reduces the numerical cost of membrane simulations a lot. In particular, the solvent-free model is more efficient for the simulations which require a large solvent space. A similar approach is also frequently used in simulations of protein folding, compare Chap. B11.

The first solvent-free model was proposed by Drouffe *et al.* [32]. In their model, a membrane is one layer of particles. It is the same length scale of coarse-graining as in the triangulated membrane models discussed in Sec. 4 below. The particles possess an orientational degree of freedom and interact with each other via three potentials: a soft-core repulsion, an anisotropic attraction, and a hydrophobic multibody interaction. Particles self-assemble into membrane patches and vesicles. A model without an orientational degree of freedom was proposed recently, and membrane properties are easy to vary [33]. These models can be applied naturally to membrane phenomena involving topological changes.

Recently, the solvent-free model was developed further to describe bilayer membranes [34, 35, 36, 37, 38]. There are several variations of the bilayer models. An amphiphilic molecule is typically modeled as a rigid or flexible chain, which consists of one hydrophilic segment and two or three hydrophobic segments. The molecules interact with each other with pairwise [36, 37, 38] or multibody [32, 34, 35] potentials. One common feature is the requirement of an attractive potential between hydrophobic segments. The bilayer models have been applied to a variety of phenomena:

- membrane fusion and fission [39, 40, 41, 35],
- pore formation in membranes [36, 42],
- the adhesion of a nanoparticle [40],
- the fluid-gel phase transition [42, 38],
- phase separation of lipids [37],
- protein inclusion in membrane [38], and
- DNA-membrane complexes [43].

In the next three subsections, we explain one of the bilayer models [34], which is well suited for the simulations of fluid membranes.

Since the solvent-free model does not take into account explicit solvent molecules, the volume of a vesicle cannot be kept constant. This is a disadvantage of this type of models. Also, hydrodynamic interactions are not present. However, these interactions can be taken into account by combining a solvent-free model with a mesoscopic solvent technique such as multi-particle collision dynamics (MPC) — which is introduced in Chap. B5.

### 3.2 Model and Simulation Methods

An amphiphilic molecule is modeled as one hydrophilic segment ( $j = 1$ ) and two hydrophobic segments ( $j = 2, 3$ ), which are separated by a fixed distance  $\sigma$  and are fixed on a line. Amphiphilic molecules ( $i = 1, \dots, N$ ) interact via a repulsive soft-core potential  $U_{\text{rep}}$  and an attractive “hydrophobic” potential  $U_{\text{hp}}$ , so that the total interaction potential is given by

$$U_{\text{am}} = \sum_{i \neq i'} U_{\text{rep}}(\sigma, |\mathbf{r}_{i,j} - \mathbf{r}_{i',j'}|) + \sum_{j=2,3} U_{\text{hp}}(\rho_{i,j}) \quad (7)$$

with

$$U_{\text{rep}}(r_0, r)/\varepsilon = \exp\{-20(r - r_0)/\sigma\}. \quad (8)$$

The multibody “hydrophobic” interaction is mimicked by a function of the local density of hydrophobic particles,

$$\rho_{i,j} = \sum_{i \neq i', j'=2,3} h(|\mathbf{r}_{i,j} - \mathbf{r}_{i',j'}|), \quad (9)$$

$$\text{where } h(r) = \frac{1}{\exp\{20(r/\sigma - 1.9)\} + 1}.$$

Thus,  $\rho_{i,j}$  is the number of hydrophobic segments in a sphere with a radius of approximately  $1.9\sigma$ . The multi-particle potential  $U_{\text{hp}}(\rho)$  is then defined by

$$U_{\text{hp}}(\rho)/\varepsilon = \begin{cases} -0.5\rho & (\rho < \rho^* - 1) \\ 0.25(\rho - \rho^*)^2 - c & (\rho^* - 1 \leq \rho < \rho^*) \\ -c & (\rho^* \leq \rho) \end{cases}, \quad (10)$$

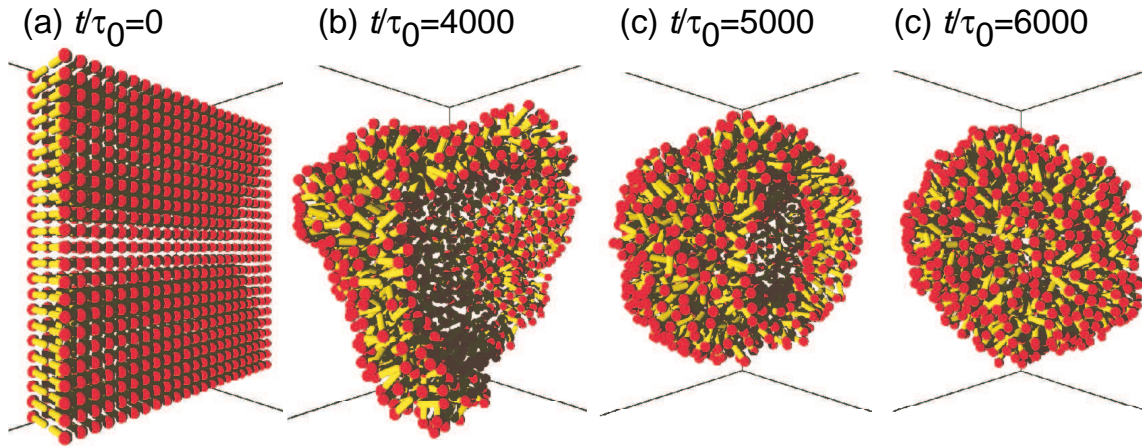


**Fig. 8:** Snapshots of a membrane to form a vesicle at  $k_B T/\varepsilon = 0.5$  and  $N = 1000$ . Red spheres and yellow cylinders represent the hydrophilic and hydrophobic segments of amphiphilic molecules, respectively.

where  $c$  is given by  $c = 0.5\rho^* - 0.25$ . The values  $\rho^* = 10$  and  $14$  are used at  $j = 2$  and  $3$ , respectively. At low density ( $\rho < \rho^* - 1$ ),  $U_{hp}(\rho)$  acts as the pair-wise potential  $-\varepsilon h(r)$ . It is assumed that the segment is shielded by hydrophobic segments from solvent molecules and hydrophilic segments at  $\rho^*$ . Thus,  $U_{hp}(\rho)$  is constant at higher density ( $\rho \geq \rho^*$ ). A similar “hydrophobic” potential is used in other solvent-free membrane and protein models. This multibody potential is employed in order to enhance the molecular diffusion in the membrane and to obtain a wide range of stability of a fluid phase. A fluid membrane is obtained by pair-wise attractive potentials [36, 37, 38]. However, the addition of density-dependence to the potentials can make the parameter range of fluid membrane much wider.

Here, we use the Brownian dynamics method (compare Chap. B4), but Monte Carlo (compare Chap. B2) or other methods are also available. The motion of the  $j$ -th segment of the  $i$ -th molecule follows the underdamped Langevin equation with the constraint of a rigid molecule:

$$m \frac{d^2 \mathbf{r}_{i,j}}{dt^2} = -\zeta \frac{d\mathbf{r}_{i,j}}{dt} + \mathbf{g}_{i,j}(t) - \frac{\partial U}{\partial \mathbf{r}_{i,j}}, \quad (11)$$

where  $m$  and  $\zeta$  are the mass and the friction constant of the segments of molecules, respectively.  $\mathbf{g}_{i,j}(t)$  is Gaussian white noise and obeys the fluctuation-dissipation theorem. The equations of the translational and the rotational motion of molecules are integrated by a leapfrog algorithm (compare Chap. B3) with a time step  $\Delta t = 0.01$ .

We present the results in units of length  $\sigma$  and time  $\tau_0 = \zeta \sigma^2 / \varepsilon$ . The mass  $m = 1$ , and the friction constant  $\zeta = 1$  of segments are fixed.  $k_B T$  is the thermal energy.

### 3.3 Properties of Vesicles

Amphiphilic molecules spontaneously form vesicles at  $N = 1000$  and  $k_B T/\varepsilon \leq 0.9$ . When the initial state is a random distribution of molecules, amphiphiles aggregate into spherical or disk-shaped micelles, which assemble and reform vesicles. When the initial state is a flat bilayer membrane, the membrane undulates by thermal fluctuation, and then bends into a vesicle

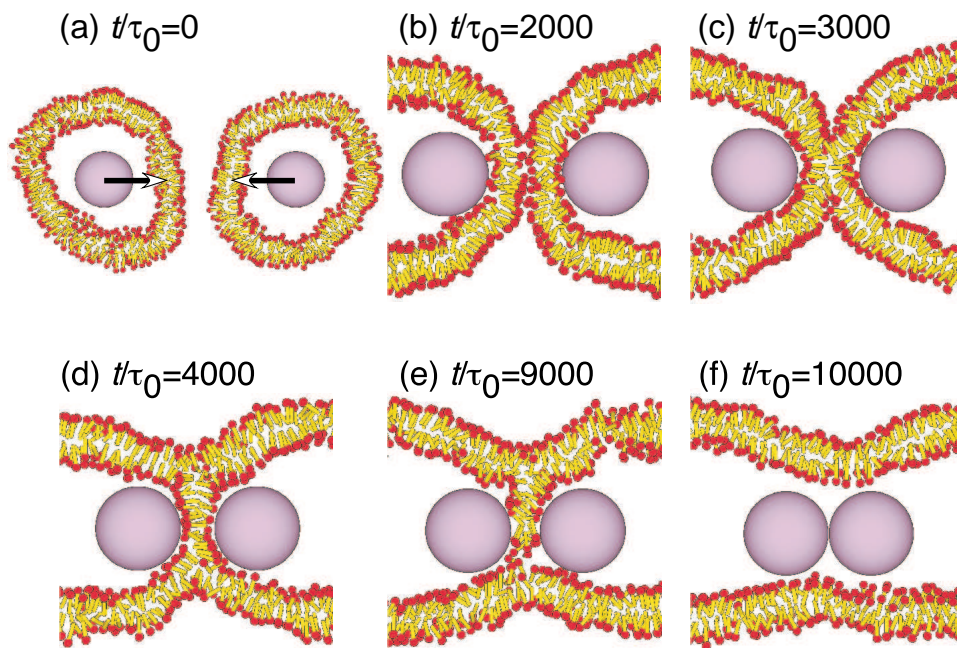


**Fig. 9:** Sliced snapshots of vesicles and two nanoparticles at the external force  $f_{\text{ex}} = 10\varepsilon/\sigma$ ,  $r_{\text{np}} = 5\sigma$ ,  $k_{\text{B}}T/\varepsilon = 0.2$ , and  $N = 4000$ . Each vesicle consists of 2000 amphiphilic molecules. Nanoparticles are placed on  $(\pm 16, 0, 0)$  at time step  $t = 0$  and are moved inside along the  $x$  axis [arrow directions in (a)] by external force. Purple spheres represent nanoparticles. The snapshots are viewed from the  $z$  direction. Molecules with  $|z/\sigma| < 2$  are shown. Modified from Ref. [35].

through a bowl-shaped conformation to reduce the length of the membrane edge [see Fig.8]. The closed-bilayer vesicles are equilibrium states under these conditions.

The vesicle exhibits a clear bilayer structure [see Fig.9] and is in a fluid phase. Molecules in vesicles diffuse laterally: the lateral diffusion constant is 0.004 at  $k_{\text{B}}T/\varepsilon = 0.2$ . The unit length  $\sigma$  corresponds to  $\sim 1\text{nm}$ . The unit time step  $\tau_0$  corresponds to  $\sim 1\text{ns}$  when the lateral diffusion constant is assumed to correspond to that of phospholipid at  $30^\circ\text{C}$ ,  $\sim 10^{-7}\text{cm}^2/\text{s}$ . The area per molecule in membranes is  $2\sigma^2$  and is larger than the experimental data for lipid molecules:  $0.4 \sim 0.8\text{nm}^2$ . A few lipid molecules are coarse-grained to one rigid molecule.

This model is designed for simulations of fluid membranes, since it has a wide temperature range where the fluid phase is stable, and a very low critical micelle concentration (CMC). The membrane properties can be varied easily by a modification of the model parameters and functional forms of the potentials. Other solvent-free models, with pair-interactions only, have been used, for example, to study gel and crystalline phases [37, 38]. Thus, the solvent-free model can be adjusted depending on the type of physical problem under investigation.

### 3.4 Membrane Fusion

The membrane fusion is a key event in various intra- and intercellular processes, such as protein trafficking, fertilization, and viral infection. However, the fusion mechanism and pathway are still unclear [44]. One of the mechanisms which has been proposed a few decades ago is the *stalk fusion model* [45]. The main idea is that when bilayers of two vesicles are brought into



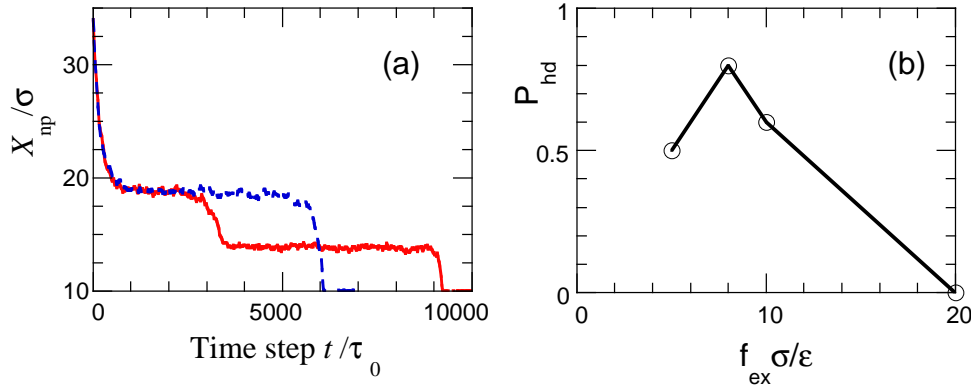


**Fig. 10:** (a) Time development of the distance  $X_{\text{np}}$  between nanoparticles. Solid red lines represent the time development for the data shown in Fig. 9. Broken blue lines represent another example. Two examples were simulated using the same parameters and initial state with different white noises. (b) Force  $f_{\text{ex}}$  dependence of the probability  $P_{\text{hd}}$  of the diaphragm pathway at  $k_{\text{B}}T/\varepsilon = 0.2$ ,  $N = 2000$ , and  $r_{\text{np}} = 3\sigma$ . Modified from Ref. [35].

contact, first the two outer monolayers connect to each other and form a “stalk intermediate”. Then, the stalk widens laterally and the two inner monolayers merge to form a new bilayer, which now separates the interior volumes of the vesicles. This bilayer is called the “hemifusion diaphragm”. The edges of the two outer monolayers also join. This state of hemifusion is a metastable state. In a second step, the hemifusion diaphragm ruptures, and the two vesicles are completely fused.

We want to discuss here the fusion of two vesicles induced by mechanical forces [35]. A nanoparticle of radius  $r_{\text{np}}$  is enclosed in each of the vesicles. The nanoparticles are fixed on the  $x$  axis at  $(X_k, 0, 0)$  with  $k = 1, 2$ , and have repulsive interaction with amphiphilic molecules and with each other. The same type of repulsive potential is used as that between amphiphilic molecules,

$$U_{\text{np}} = \sum_{i,j} U_{\text{rep}}(\sigma/2 + r_{\text{np}}, |\mathbf{r}_{i,j} - \mathbf{r}_{\text{np}}|) + U_{\text{rep}}(2r_{\text{np}}, X_1 - X_2) \quad (12)$$

Each nanoparticle is placed at the center of mass of a vesicle and is moved by a constant external force  $f_{\text{ex}}$  to the arrow direction in Fig. 9(a). The motion of the nanoparticles follows the underdamped Langevin equation with the mass  $m$  and the friction constant  $\zeta_{\text{np}} = 300\zeta$ . The unit of external force  $\varepsilon/\sigma$  is  $\sim 20\text{pN}$ .

Figures 9 and 10(a) show examples of the fusion process. Two vesicles dragged by nanoparticles come into contact [Fig. 9(b)]. In some runs, the vesicles fuse directly after trans-monolayer contact [Fig. 9(c)]. In the other runs, the vesicles form a disk-shaped bilayer consisting of both inner monolayers [Fig. 9(d)], which agrees with the hemifusion diaphragm in the original stalk fusion model. A fusion pore then opens at the *edge* of the hemifusion diaphragm [Fig. 9(e)]. We call the former a direct pathway and the latter a diaphragm pathway. The distances  $X_{\text{np}}$  for two, one, and no bilayer between nanoparticles are  $20\sigma$ ,  $15\sigma$ , and  $10\sigma$ , respectively, because the bilayer thickness is  $5\sigma$  [Fig. 10(a)]. The fusion stochastically occurs through direct or diaphragm pathways. The probability of diaphragm pathway has a maximum  $P_{\text{hd}} = 0.8$  at  $f_{\text{ex}}\sigma/\varepsilon = 8$  [Fig. 10(b)]. Larger forces break the bilayer diaphragm more quickly. Under weaker forces, the nanoparticles expand the trans-monolayer contact more weakly. Therefore,

$P_{\text{hd}}$  decreases in both cases. The above fusion pathways are different with those of spontaneous fusion [39], where fusion occurs via a stalk intermediate. Thus, the perturbation due to the force of the nanoparticles changes the fusion pathway.

## 4 Dynamically-Triangulated Surfaces

### 4.1 Continuum Description and Curvature Elasticity

The simulation of membranes and vesicles with characteristic sizes on the order of 100 nm to 10  $\mu\text{m}$  is impossible on the basis of a molecular model, since it would require an enormous number of lipid and solvent molecules. Therefore, on this coarse-graining level, a model is necessary in which the individual lipid molecules are no longer “visible”. Instead, the membrane is described by a mathematical surface with an elastic energy is most appropriate on these mesoscopic length scales [1, 3, 5]. In this case, the bilayer is described by a mathematical surface. The shapes and fluctuations of this surface are controlled by the curvature elastic energy [46, 47]

$$\mathcal{H}_{\text{curv}} = \int dS [\gamma + 2\kappa(H - C_0)^2 + \bar{\kappa}K + \dots] \quad (13)$$

where integral extends over the whole membrane surface. The shape of the membrane is expressed by the two principal curvatures  $c_1$  and  $c_2$  — the two eigenvalues of the curvature tensor [48] — at each point of the membrane, which appear in the Hamiltonian (13) as

$$H = [c_1 + c_2]/2 \quad , \quad K = c_1 c_2 \quad , \quad (14)$$

the mean and Gaussian curvatures, respectively. The parameters of the curvature energy are the surface tension  $\gamma$ , the bending rigidity  $\kappa$ , the saddle-splay modulus  $\bar{\kappa}$  and the spontaneous curvature  $C_0$ . These elastic constants of the membrane are the only place where the chemistry, the molecular architecture and the interactions of the constituent lipid and protein molecules enter into this model.

### 4.2 Simulation Method

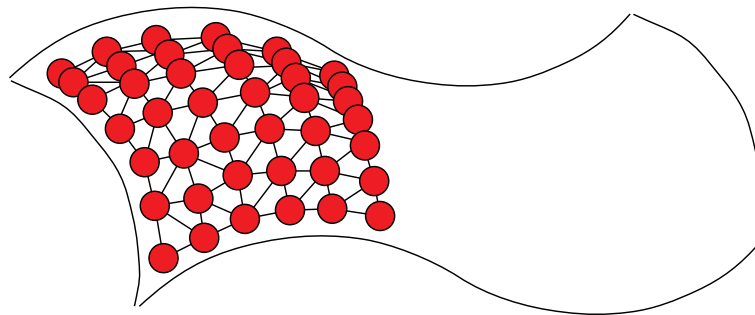
In order to make this model suitable for simulations, the continuous surface has to be approximated by a network of vertices and bonds, see Fig. 11. A triangular network is usually used because it provides the most homogeneous and isotropic discretization of the surface [49]. The simplest potential for the interaction of vertices which are connected by bonds is a *tethering potential*,

$$V(r) = \begin{cases} 0 & \text{if } r < \ell_0 \\ \infty & \text{otherwise} \end{cases} \quad (15)$$

which causes the particles to behave as tethered by a string.

When hard spheres of diameter  $\sigma_0$  are placed on the vertices, and the bond lengths  $\ell_0$  are restricted to be  $\ell_0 \leq \sqrt{3}\sigma_0$ , the surface is *self-avoiding*, since an arbitrary sphere does *not* fit through the holes of the network, so that no interpenetration of different parts of the network is possible.

### Dynamically triangulated surfaces



Hard-core diameter  $\sigma$

Tether length  $L$ :  $\sigma < L < \sqrt{3}\sigma$

--> self-avoidance

Dynamic triangulation:

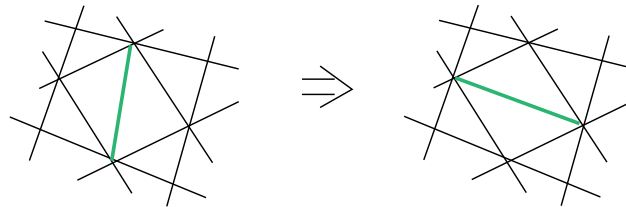


**Fig. 11:** A triangulated network model of a fluctuating surface. *Top:* Hard spheres connected by bonds of maximum extension  $\ell_0$  are used to describe self-avoiding membranes. *Bottom:* The Monte Carlo step, which makes the triangulation dynamic, is required to model fluid membranes.



The energy, which appears in the Boltzmann weight is the curvature energy, which can be discretized in the form [50, 51]

$$E_b = \lambda_b \sum_{\langle ij \rangle} (1 - \mathbf{n}_i \cdot \mathbf{n}_j) \quad (16)$$

where  $\mathbf{n}_i$  and  $\mathbf{n}_j$  are the normal vectors of neighboring triangles, and the sum runs over all pairs of neighboring triangles. The coupling constant  $\lambda_b$  in Eq. (16) is related to the bending rigidity and saddle-splay modulus (see Sec. 4.1 below) by  $\kappa = \sqrt{3}\lambda_b/2$  and  $\bar{\kappa} = -\kappa$  [52]. The discretization (16) of the curvature energy is not without problems; better discretizations are discussed in Ref. [53].

**Polymerized Membranes** — Membranes, in which neighboring particles are chemically linked together are called polymerized. Examples of such membranes are the graphite monolayers which are found in fullerenes, or the polymer network attached to the inside of the lipid membranes of red blood cells, .

Triangulated surface models for polymerized membranes have first been suggested and studied by Monte Carlo simulations in 1987 [50, 51] and 1988 [54], and by molecular dynamics simulations in 1989 [55]. Since then, the properties of triangulated surfaces of fixed triangulation have been investigated intensively, see e.g. the reviews [49].

A Monte Carlo step consists of a random displacement of a randomly selected vertex. This step is accepted with the probability determined by the Boltzmann weight with energy 16, as long as the vertices remain within the maximum bond lengths with their neighbors. In molecular dynamics simulations, a smooth bond potentials are usually employed, compare Ref. [55].

**Fluid Membranes** — For a study of fluid membranes, the connectivity of the membrane vertices cannot remain fixed during the simulation, because otherwise a diffusion of vertices within the membrane is not possible. Therefore, dynamically triangulated surfaces [56, 57, 58] have to be used in this case. The essential step of the dynamic triangulation procedure is shown at the bottom of Fig. 11. Among the four vertices of two neighboring triangles, the “diagonal” bond is switched from one of the two possible positions to the other. This bond-switching is only allowed if the vertices remain connected to at least three neighbors after the switch. Also, the distance between the newly connected vertices has to be smaller than the maximum bond length. This Monte Carlo step has the advantages that

- it is local, i.e. only the vertices of two neighboring triangles are involved, and
- it guarantees that the network retains its two-dimensional connectivity during the whole simulation run.

[49, 59]

### 4.3 Crumpling of Thin Elastic Sheets

The crumpling of a sheet of paper is an everyday experience. However, although everybody has probably noticed the intriguing pattern of folds, which can be seen on a sheet of paper, which has been crumpled and then smoothened out by hand, crumpling has come into scientific focus only very recently. The key observation was here that the properties of a single fold — also called a *stretching ridge* — can be understood very well from the balance of bending and stretching energies [60]. Simulations at zero temperature, i.e. energy minimization of tethered membranes of tetrahedral and icosahedral topology have played an important role in



**Fig. 12:** *Typical conformation of a crumpled self-avoiding thin sheet. The tethered network of originally flat, circular shape has been crumpled inside a spherical shell to 42% of its original linear size. The formation of folds under compression is clearly visible. Picture courtesy of G. Vliegenthart (FZ Jülich).*

understanding the scaling properties of these single folds as a function of the fold length, the bending rigidity and the shear modulus [60, 61].

Much less is known so far about the properties of crumpled sheets. In the simulations, a tethered network of circular shape is enclosed inside a spherical shell. The radius of the shell is then slowly reduced under an external pressure until a final state is reached, at which the external forces are balanced by the elastic forces of the sheet. Such simulations have been performed both for phantom sheets (in which different parts of the membrane can interpenetrate without energy cost) [62], as well as for self-avoiding sheets [63]. A typical conformation of a self-avoiding sheet is shown in Fig. 12. The simulations can help to answer many questions, such as: How does the elastic force of the sheet increase with decreasing radius? Is there a difference between phantom and self-avoiding sheets? How can the fold pattern be characterized? What is the distribution of fold lengths?

As an example for the results obtained in the simulations, Fig. 13 shows the distribution of fold lengths for both phantom and self-avoiding sheets. The simulations show that there is a very broad distribution of fold lengths, with many more short folds than long folds. This is in excellent agreement with experimental observations for crumpled paper [64]. Furthermore, self-avoiding sheets have much more folds than phantom sheets, because phantom sheets have more freedom to find a configuration of minimal bending and stretching energy.

#### 4.4 Vesicles and Red Blood Cells in Capillary Flow

The rheological properties of red blood cells (RBCs) are among the key factors for the flow resistance of blood in micro-vessels, since the half volume of normal human blood is filled with RBCs. Human RBCs have a biconcave-disk shape with a diameter of  $8\mu\text{m}$  under physiological conditions. Because of the large surface area  $S$  compared to a sphere of equal volume  $V$ , RBCs

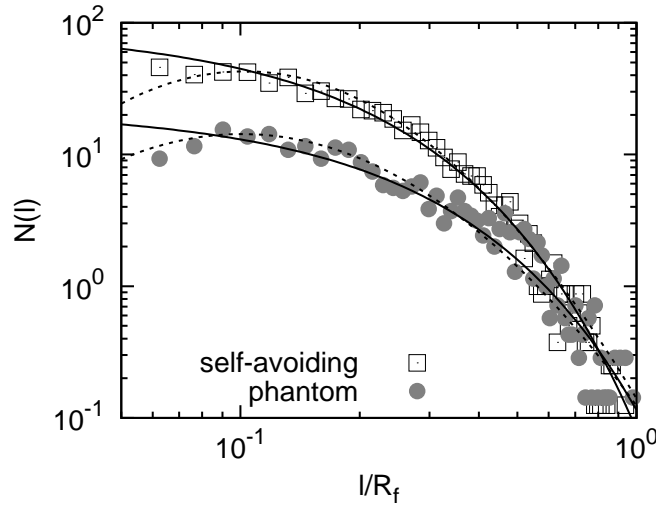


**Fig. 13:** Distribution  $N(l)$  of fold lengths for both phantom and self-avoiding sheets. The fold lengths  $l$  are scaled by the radius  $R_f$  of the enclosing sphere. The compression of the sheet is  $R_f/R_0 = 0.18$ . The solid and dashed lines are fits to exponential and log-normal distributions. Modified from Ref. [63].

are easily deformed by external forces. However, in diseases such as diabetes mellitus, RBCs have reduced deformability, and the apparent viscosity increases. We simulated a vesicle and RBC in cylindrical capillary flow using the combination of a dynamically-triangulated surface model and multi-particle collision dynamics (MPC) for the solvent [65].

The triangulated-network model introduced above has to be slightly modified in order to combine it with MPC. Since the temporal evolution of the positions of the membrane vertices is determined by Newton's equation of motion, soft pairwise potentials are employed for the tether-bond and excluded volume. The volume  $V$  and surface area  $S$  of a vesicle are kept constant by constraint potentials. The membrane viscosity is varied by changing the bond-flip rate, where the membrane viscosity increasing with decreasing number of bond-flips per time step. We use the reduced volume  $V^* = V/(4\pi R_0^3/3) = 0.59$ , where  $R_0 = \sqrt{S/4\pi}$  is the effective vesicle radius. At this reduced volume, a biconcave discocyte is the equilibrium shape, and a prolate ellipsoid and stomatocyte are metastable in the absence of flow [66]. The RBC membrane is modeled as a composite network, which consists of a dynamically-triangulated surface as in the case of fluid vesicles, coupled to an additional network of harmonic springs with fixed connectivity (no bond-switching). The same number of the bonds is used for both the fluid and the tethered networks.

The details of the MPC method are explained in Chap. B5. The solvent is described by point-like particles. The MPC algorithm consists of alternating streaming and collision steps. In the streaming step, the particles move ballistically. In the collision step, the particles are sorted into cubic boxes. The collision step consists of a stochastic rotation of the relative velocities of each particle in a box. The solvent particles interact with the membrane in two ways. First, the membrane vertices are included in the MPC collision procedure. Second, the solvent particles are scattered with a bounce-back rule from membrane triangles. These interactions together ensure that the fluid satisfies a no-slip boundary condition on the membrane. The fluids in the interior and exterior of the vesicle are taken to be the same, in particular to have the same

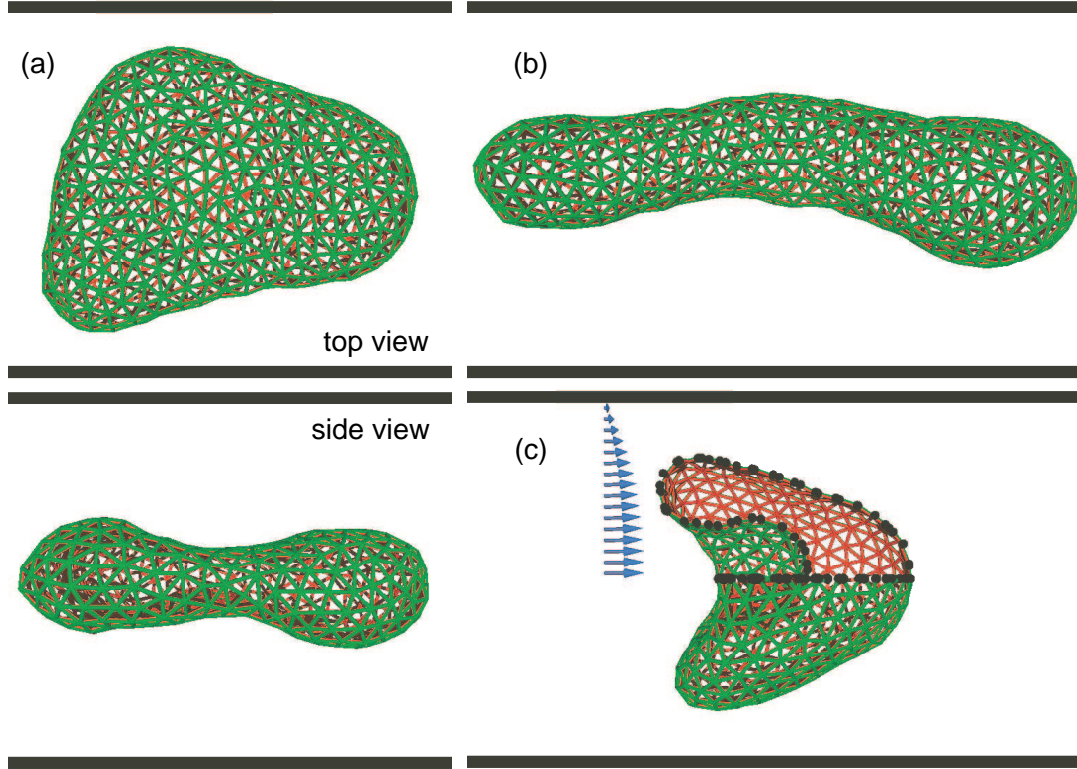


**Fig. 14:** Snapshots of vesicles in capillary flow (with bending rigidity  $\kappa/k_B T = 20$ ). (a) Fluid vesicle with discoidal shape at the mean fluid velocity  $v_m \tau / R_{\text{cap}} = 41$ , both in side and top views. (b) Fluid vesicle with prolate shape at  $v_m \tau / R_{\text{cap}} = 69$ . (c) Elastic vesicle (RBC model) with parachute shape at  $v_m \tau / R_{\text{cap}} = 218$  (with shear modulus  $\mu R_0^2 / k_B T = 110$ ). The membrane consists of  $N_{\text{mb}} = 500$  vertices. The blue arrows represent the velocity field of the solvent. The upper front quarter of the vesicle in (c) are removed to allow a look into the interior; the black circles indicate the lines where the membrane has been cut in this procedure. Thick black lines indicate the walls the cylindrical capillary.

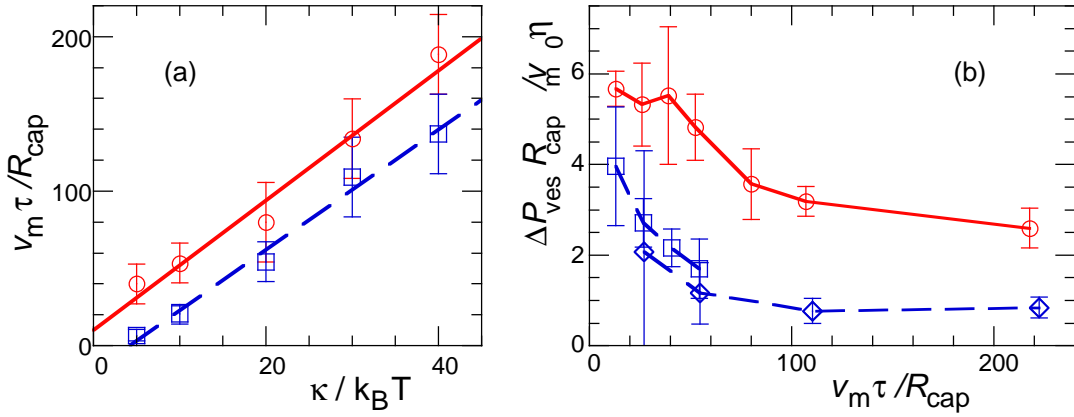


**Fig. 15:** (a) Dependence of the shape-transition velocity on the bending rigidity  $\kappa$ . Transitions of elastic vesicles (with  $\mu R_0^2/k_B T = 110$ ) from disk to parachute ( $\circ$ ), as well as transitions of fluid vesicles from disk to prolate ( $\square$ ) are shown. Solid and broken lines are linear fits to the data. (b) flow resistance  $\Delta P_{\text{ves}}/v_m$  per vesicle, for  $\kappa/k_B T = 20$  and  $\mu R_0^2/k_B T = 110$ . The solid and broken lines correspond to elastic and fluid vesicles, respectively. Data are shown for discoidal vesicles ( $\square$ ) and prolate-ellipsoidal vesicles ( $\diamond$ ). Modified from Ref. [65].

viscosity  $\eta_0$ .

In experimental conditions of RBCs, the Reynolds number  $\text{Re} = \rho v_{\text{ves}} R_0 / \eta_0$  is very small, typically  $\text{Re} \simeq 10^{-2}$ , where  $v_{\text{ves}}$  is the mean velocity of the vesicle. Therefore, we chose parameters such that  $\text{Re} < 1$  in all simulations. We use a capillary radius of  $R_{\text{cap}} = 1.4 R_0$ , which corresponds to the narrow capillaries in the human body. The results are scaled with the intrinsic relaxation time  $\tau = \eta_0 R_{\text{cap}}^3 / k_B T$ .

Both fluid and elastic vesicles retain their discoidal shapes in slow capillary flows [see Figs. 14(a)]. The vesicles align the longest axis of the gyration tensor with the flow direction, even if their initial conformations are coaxial with the capillary. The discoidal shape is elongated in the flow direction and its front-rear symmetry is broken, but the biconcave dimples and the mirror symmetry with respect to the plane determined by the two eigenvectors of the gyration tensor with the largest eigenvalues are retained.

At large mean fluid velocity, the fluid vesicle transits into a prolate ellipsoidal shape [see Fig. 14(b)], since this shape change reduces the flow resistance. On the other hand, the elastic vesicle transits into a parachute shape, [see Fig. 14(c)], since the shear elasticity prevents the elongation of the vesicle into a prolate shape in this case.

The mean fluid velocities  $v_m$  at both shape transitions are found to increase linearly with the bending rigidity  $\kappa$  of the membrane, see Fig. 15(a). Since the data extrapolate to a very small flow velocity in the limit  $\kappa/k_B T \rightarrow 0$ , we conclude that  $\kappa$  is the dominant factor in determining the transition velocity in the regime  $\mu R_0^2/k_B T \leq 110$ . At fixed bending rigidity  $\kappa/k_B T = 10$ , the transition velocity is found to increase also roughly linearly with increasing shear elasticity. Based on these linearity, we can predict that parachute shapes of RBCs should appear for flow velocities larger than  $800 R_{\text{cap}} / \tau \simeq 0.2 \text{ mm/s}$  under physiological conditions. This is consistent with the experimental results of Ref. [67], and is in the range of micro-circulation in the human body.

Figure 15(b) shows the flow resistance  $\Delta P_{\text{ves}}/v_m$  in the capillary. The pressure drop  $\Delta P_{\text{ves}}$  per vesicle is calculated by  $\Delta P_{\text{ves}} = 8\eta_0(v_0 - v_m)L_z/R_{\text{cap}}^2$ , where  $v_0$  is the mean fluid velocity in

absence of vesicle and  $L_z$  is the length of the capillary. This expression is obtained from the well-known result of the pressure drop in simple Poiseuille flow,  $\partial P/\partial z = -4\eta_0 v_{\max}/R_{\text{cap}}^2$ , where for a parabolic velocity profile the maximum velocity  $v_{\max}$  at the center of capillary is related to the mean velocity  $v_0$  by  $v_{\max} = 2v_0$ . In the presence of the vesicle, there is an extra pressure drop, so that  $\Delta P = \Delta P_{\text{ves}} + 8\eta_0 v_m L_z/R_{\text{cap}}^2$ . The flow resistance decrease with increasing  $v_m$ , with jumps at the shape transitions. Thus, both shape transitions reduce the flow resistance.

The dynamics of vesicles in simple shear flow has also been studied using this method [68, 69]. Several types of shape transitions were found, which are accompanied by changes of the dynamical behavior.

## Appendices

### A Thermal Fluctuations of Nearly Planar Membranes

In the limit of small deflections from a planar reference state, an analytical calculation of the fluctuation spectrum of membranes is possible. In this case, the Monge representation can be employed, where a height-field  $h(\mathbf{r})$  describes the local membrane position. If the deviations from the planar reference state are sufficiently small, an expansion in powers of  $|\nabla h|$  is justified. To leading order in this expansion, the curvature energy becomes

$$E_b \simeq \int d^2x \left[ \frac{\gamma}{2} (\nabla h(\mathbf{x}))^2 + \frac{\kappa}{2} (\nabla^2 h(\mathbf{x}))^2 \right]. \quad (17)$$

Here, the first term, which is proportional to the surface tension  $\gamma$ , is obtained from an expansion of the excess surface area [48],  $\int d^2x [(1 + (\nabla h)^2)^{1/2} - 1]$ , to leading order in  $\nabla h$ .

In Fourier space, with

$$h(\mathbf{x}) = \int \frac{d^2q}{(2\pi)^2} h(\mathbf{q}) e^{i\mathbf{q}\cdot\mathbf{x}} \quad (18)$$

the expressions in Eq. (17) simplify to

$$\begin{aligned} \int d^2x (\nabla^n h(\mathbf{x}))^2 &= \\ &= \int \frac{d^2q}{(2\pi)^2} \int \frac{d^2q'}{(2\pi)^2} (-q^n)(-q'^n) h(\mathbf{q}) h(\mathbf{q}') \underbrace{\int d^2x e^{i(\mathbf{q}+\mathbf{q}')\cdot\mathbf{x}}}_{(2\pi)^2 \delta(\mathbf{q}+\mathbf{q}')} \\ &= \int \frac{d^2q}{(2\pi)^2} q^{2n} |h(\mathbf{q})|^2 \end{aligned} \quad (19)$$

with  $n = 1$  for the surface-tension term and  $n = 2$  for the curvature terms, where

$$h(-\mathbf{q}) = h^*(\mathbf{q}) \quad (20)$$

since  $h(\mathbf{r}) \in \mathbb{R}$ . Therefore we finally obtain

$$E_b = \int \frac{d^2q}{(2\pi)^2} \left[ \frac{\gamma}{2} q^2 + \frac{\kappa}{2} q^4 \right] |h(\mathbf{q})|^2 \quad (21)$$

This is an important result, since it shows that the fluctuation modes, which are called *undulation modes* for membranes, *decouple* in Fourier space. The calculation of the fluctuation spectra then becomes very simple, since the *equipartition theorem* — which states that the energy of each independent mode is  $k_B T/2$  on average — then implies

$$\langle h(\mathbf{q}) h(\mathbf{q}') \rangle = \frac{k_B T}{\gamma q^2 + \kappa q^4} \delta(\mathbf{q} + \mathbf{q}') \quad (22)$$

## References

- [1] G. Gompper and M. Schick, in *Phase Transitions and Critical Phenomena*, edited by C. Domb and J. Lebowitz (Academic Press, London, 1994), vol. 16, pp. 1–176.
- [2] W. M. Gelbart, A. Ben-Shaul, and D. Roux, eds., *Micelles, Membranes, Microemulsions, and Monolayers* (Springer-Verlag, Berlin, 1994).
- [3] S. A. Safran, *Statistical Thermodynamics of Surfaces, Interfaces, and Membranes* (Addison-Wesley, Reading, MA, 1994).
- [4] R. Lipowsky and E. Sackmann, eds., *Structure and dynamics of membranes - from cells to vesicles*, vol. 1 of *Handbook of biological physics* (Elsevier, Amsterdam, 1995).
- [5] D. Nelson, T. Piran, and S. Weinberg, eds., *Statistical Mechanics of Membranes and Surfaces* (World Scientific, Singapore, 2004), 2nd ed.
- [6] K. Simons and E. Ikonen, *Nature* **387**, 569 (1997).
- [7] D. Voet and J. G. Voet, *Biochemistry* (Wiley, New York, 1995), 2nd ed.
- [8] S. Karaborni and B. Smit, *Curr. Opin. Colloid Interface Sci.* **1**, 411 (1996).
- [9] R. G. Larson, *Curr. Opin. Colloid Interface Sci.* **2**, 361 (1997).
- [10] D. J. Tobias, K. Tu, and M. L. Klein, *Curr. Opin. Colloid Interface Sci.* **2**, 15 (1997).
- [11] S. Bandyopadhyay, M. Tarek, and M. L. Klein, *Curr. Opin. Colloid Interface Sci.* **3**, 242 (1998).
- [12] J. C. Shelley and M. Y. Shelley, *Curr. Opin. Colloid Interface Sci.* **5**, 101 (2000).
- [13] D. P. Tieleman, S. J. Marrink, and H. J. C. Berendsen, *Biochim. Biophys. Acta* **1331**, 235 (1997).
- [14] E. S. Boek, W. K. den Otter, W. J. Briels, and D. Iakovlev, *Phil. Trans. R. Soc. Lond. A* **362**, 1625 (2004).
- [15] R. Goetz and R. Lipowsky, *J. Chem. Phys.* **108**, 7397 (1998).
- [16] R. Goetz, G. Gompper, and R. Lipowsky, *Phys. Rev. Lett.* **82**, 221 (1999).
- [17] J. C. Shillcock and R. Lipowsky, *J. Chem. Phys.* **117**, 5048 (2002).
- [18] W. K. den Otter and W. J. Briels, *J. Chem. Phys.* **118**, 4712 (2003).
- [19] G. Srinivas, D. E. Disher, and M. L. Klein, *Nature Materials* **3**, 638 (2004).
- [20] V. Ortiz, S. O. Nielsen, D. E. Discher, M. L. Klein, R. Lipowsky, and J. Shillcock, *J. Phys. Chem. B* **109**, 17708 (2005).
- [21] G. Illya, R. Lipowsky, and J. C. Shillcock, *J. Chem. Phys.* **122**, 244901 (2005).
- [22] M. Kranenburg, M. Venturoli, and B. Smit, *Phys. Rev. E* **67**, 060901 (2003).



- [23] R. D. Groot and K. L. Rabone, *Biophys. J.* **81**, 725 (2001).
- [24] T. V. Tolpekina, W. K. den Otter, and W. J. Briels, *J. Chem. Phys.* **121**, 8014 (2004).
- [25] W. K. den Otter, *J. Chem. Phys.* **123**, 214906 (2005).
- [26] M. Laradji and P. B. S. Kumar, *Phys. Rev. Lett.* **93**, 198105 (2004).
- [27] M. Müller, K. Katsov, and M. Schick, *Biophys. J.* **85**, 1611 (2003).
- [28] M. J. Stevens, J. H. Hoh, and T. B. Woolf, *Phys. Rev. Lett.* **91**, 188102 (2003).
- [29] S. J. Marrink and A. E. Mark, *J. Am. Chem. Soc.* **125**, 11144 (2003).
- [30] J. C. Shillcock and R. Lipowsky, *Nature Materials* **4**, 225 (2005).
- [31] D. W. Li and X. Y. Liu, *J. Chem. Phys.* **122**, 174909 (2005).
- [32] J. M. Drouffe, A. C. Maggs, and S. Leibler, *Science* **254**, 1353 (1991).
- [33] H. Noguchi and G. Gompper, *Phys. Rev. E* **73**, 021903 (2006).
- [34] H. Noguchi and M. Takasu, *Phys. Rev. E* **64**, 041913 (2001).
- [35] H. Noguchi, *J. Chem. Phys.* **117**, 8130 (2002).
- [36] O. Farago, *J. Chem. Phys.* **119**, 596 (2003).
- [37] I. R. Cooke, K. Kremer, and M. Deserno, *Phys. Rev. E* **72**, 011506 (2005).
- [38] G. Brannigan, L. C. L. Lin, and F. L. H. Brown, *Eur. Biophys. J.* **35**, 104 (2006).
- [39] H. Noguchi and M. Takasu, *J. Chem. Phys.* **115**, 9547 (2001).
- [40] H. Noguchi and M. Takasu, *Biophys. J.* **83**, 299 (2002).
- [41] H. Noguchi and M. Takasu, *Phys. Rev. E* **65**, 051907 (2002).
- [42] I. R. Cooke and M. Deserno, *J. Chem. Phys.* **123**, 224710 (2005).
- [43] O. Farago, N. Grønbech-Jensen, and P. Pincus, *Phys. Rev. Lett.* **96**, 018102 (2006).
- [44] R. Jahn and H. Grubmüller, *Curr. Opin. Cell Biol.* **14**, 488 (2002).
- [45] V. S. Malinin and B. R. Lentz, *Biophys. J.* **86**, 2951 (2004).
- [46] P. B. Canham, *J. Theor. Biol.* **26**, 61 (1970).
- [47] W. Helfrich, *Z. Naturforsch.* **28c**, 693 (1973).
- [48] E. Kreyszig, *Differential Geometry* (Dover Publications, New York, 1991).
- [49] G. Gompper and D. M. Kroll, *J. Phys.: Condens. Matter* **9**, 8795 (1997).
- [50] Y. Kantor and D. R. Nelson, *Phys. Rev. Lett.* **58**, 2774 (1987).

- [51] Y. Kantor and D. R. Nelson, Phys. Rev. A **36**, 4020 (1987).
- [52] H. S. Seung and D. R. Nelson, Phys. Rev. A **38**, 1005 (1988).
- [53] G. Gompper and D. M. Kroll, J. Phys. I France **6**, 1305 (1996).
- [54] M. Plischke and D. Boal, Phys. Rev. A **38**, 4943 (1988).
- [55] F. F. Abraham, W. E. Rudge, and M. Plischke, Phys. Rev. Lett. **62**, 1757 (1989).
- [56] J.-S. Ho and A. Baumgärtner, Europhys. Lett. **12**, 295 (1990).
- [57] D. M. Kroll and G. Gompper, Science **255**, 968 (1992).
- [58] D. H. Boal and M. Rao, Phys. Rev. A **45**, R6947 (1992).
- [59] G. Gompper and D. M. Kroll, in *Statistical Mechanics of Membranes and Surfaces*, edited by D. R. Nelson, T. Piran, and S. Weinberg (World Scientific, Singapore, 2004), pp. 359–426, 2nd ed.
- [60] A. Lobkovsky, S. Gentges, H. Li, D. Morse, and T. A. Witten, Science **270**, 1482 (1995).
- [61] Z. Zhang, H. T. Davis, R. S. Maier, and D. M. Kroll, Phys. Rev. B **52**, 5404 (1995).
- [62] E. M. Kramer and T. A. Witten, Phys. Rev. Lett. **78**, 1303 (1997).
- [63] G. Vliegenthart and G. Gompper, Nature Materials, doi:10.1038/nmat1581 (2006).
- [64] D. L. Blair and A. Kudrolli, Phys. Rev. Lett. **94**, 166107 (2005).
- [65] H. Noguchi and G. Gompper, Proc. Natl. Acad. Sci. USA **102**, 14159 (2005).
- [66] U. Seifert, Adv. Phys. **46**, 13 (1997).
- [67] Y. Suzuki, N. Tateishi, M. Soutani, and N. Maeda, Microcirc. **3**, 49 (1996).
- [68] H. Noguchi and G. Gompper, Phys. Rev. Lett. **93**, 258102 (2004).
- [69] H. Noguchi and G. Gompper, Phys. Rev. E **72**, 011901 (2005).